Original Article

MOLECULAR METABOLISM

Depletion of pyruvate kinase (PK) activity causes glycolytic intermediate imbalances and reveals a PK-TXNIP regulatory axis

Anna Nieborak [1], Saulius Lukauskas [1], Jordi Capellades [4,5], Patricia Heyn [1], Gabriela Silva Santos [1], Karsten Motzler [6,7,8], Anja Zeigerer [6,7,8], Romina Bester [9], Ulrike Protzer [9], Florian Schelter [10], Mirko Wagner [10], Thomas Carell [10], Alexander Hruscha [3], Bettina Schmid [3], Oscar Yanes [4,5], Robert Schneider [1,2,*]

ABSTRACT

Objective: Cancer cells convert more glucose into lactate than healthy cells, what contributes to their growth advantage. Pyruvate kinase (PK) is a key rate limiting enzyme in this process, what makes it a promising potential therapeutic target. However, currently it is still unclear what consequences the inhibition of PK has on cellular processes. Here, we systematically investigate the consequences of PK depletion for gene expression, histone modifications and metabolism.

Methods: Epigenetic, transcriptional and metabolic targets were analysed in different cellular and animal models with stable knockdown or knockout of PK.

Results: Depleting PK activity reduces the glycolytic flux and causes accumulation of glucose-6-phosphate (G6P). Such metabolic perturbation results in stimulation of the activity of a heterodimeric pair of transcription factors MondoA and MLX but not in a major reprogramming of the global H3K9ac and H3K4me3 histone modification landscape. The MondoA:MLX heterodimer upregulates expression of thioredoxin-interacting protein (TXNIP) — a tumour suppressor with multifaceted anticancer activity. This effect of TXNIP upregulation extends beyond immortalised cancer cell lines and is applicable to multiple cellular and animal models.

Conclusions: Our work shows that actions of often pro-tumorigenic PK and anti-tumorigenic TXNIP are tightly linked via a glycolytic intermediate. We suggest that PK depletion stimulates the activity of MondoA:MLX transcription factor heterodimers and subsequently, increases cellular TXNIP levels. TXNIP-mediated inhibition of thioredoxin (TXN) can reduce the ability of cells to scavenge reactive oxygen species (ROS) leading to the oxidative damage of cellular structures including DNA. These findings highlight an important regulatory axis affecting tumour suppression mechanisms and provide an attractive opportunity for combination cancer therapies targeting glycolytic activity and ROS-generating pathways.

Keywords Pyruvate kinase; Cancer; ROS; Glycolysis; Thioredoxin-interacting protein; Arrestins; Metabolic flux

1. INTRODUCTION

Cancer cells usually adapt their metabolism to support tumour growth and outgrow healthy cells [1]. While non-transformed cells preferentially obtain energy (in the form of adenosine triphosphate (ATP)) from mitochondrial oxidative phosphorylation, transformed cancerous cells often shift their metabolism towards glycolysis, regardless of the availability of oxygen [2], a phenomenon known as the 'Warburg effect' [3,4]. In line with this, overexpression of genes involved in glucose uptake and glycolysis are hallmarks of many cancers including breast, liver, colon, kidney, lung, pancreas and stomach cancers [5,6]. These cancer cells are characterised by an increased need for glycolytic metabolites that provide 'building blocks' for macromolecules necessary for cell proliferation and division. Multiple anti-glycolytic agents are currently studied as potential anticancer therapies [7].

Pyruvate kinase (PK) is an enzyme with a crucial importance for cellular metabolism and homeostasis of the whole organism. Its pivotal role in glucose catabolism is the catalysis of the final and rate-limiting

[1]Institute of Functional Epigenetics, Helmholtz Zentrum München, 85764 Neuherberg, Germany [2]Faculty of Biology, Ludwig-Maximilians-Universität München, 82152 Planegg-Martinsried, Germany [3]German Center for Neurodegenerative Diseases (DZNE) Munich, 81377 Munich, Germany [4]Universitat Rovira i Virgili, Department of Electronic Engineering, IISPV, Tarragona, Spain [5]CIBER on Diabetes and Associated Metabolic Diseases (CIBERDEM), Instituto de Salud Carlos III, Madrid, Spain [6]Institute for Diabetes and Cancer, Helmholtz Center Munich, 85764 Neuherberg, Germany [7]German Center for Diabetes Research (DZD), 85764 Neuherberg, Germany [8]Joint Heidelberg-IDC Translational Diabetes Program, Inner Medicine 1, Heidelberg University Hospital, Heidelberg, Germany [9]Institute of Virology, Technical University of Munich, School of Medicine/Helmholtz Munich, Trogerstr. 30, 81675 Munich, Germany [10]Ludwig-Maximilians-Universität München, Institute for Chemical Epigenetics Munich, Butenandtstr. 5-13, 81377 Munich, Germany

*Corresponding author. Institute of Functional Epigenetics, Helmholtz Zentrum München, 85764 Neuherberg, Germany. E-mail: robert.schneider@helmholtz-muenchen.de (R. Schneider).

Received January 19, 2023 • Revision received May 14, 2023 • Accepted May 31, 2023 • Available online 7 June 2023

https://doi.org/10.1016/j.molmet.2023.101748

reaction of the glycolysis pathway by converting highly energetic phosphoenolpyruvate to pyruvate with concomitant generation of ATP. In mammals, there are two genes encoding for a total of four isoforms of PK. The PKLR gene encodes for the PKL and PKR isoforms. PKL, is mainly expressed in liver and PKR is expressed exclusively in erythrocytes. PKM1 and PKM2 are formed by alternative splicing of the PKM transcript and their expression pattern is less clearly defined and can vary in response to external stimuli, stress or disease [8,9]. PKM2 is prone to allosteric regulation due to the inclusion of exon 10 into this isoform, as opposed to exon 9 into PKM1. PKM2 can be found either as a highly active tetramer or a low-activity dimer [10–12]. Dimeric PKM2 can, upon exposure to certain stimuli, localise to the nucleus and serve as a transcriptional coactivator of genes involved in proliferation and glycolysis. It thereby provides a positive feedback loop leading to uncontrolled cell proliferation [13–18]. Switching from the expression of PKM2 to PKM1 can reverse the Warburg effect in different cancer cell lines and reduce tumour growth [19]. However, this view of PKM2 being the main PK isoform responsible for tumorigenesis has been recently challenged by Morita et al. by showing that only cells expressing exclusively PKM1, but not exclusively PKM2, promote tumour growth in mouse transplantation model [20]. Cancer cells can also adapt their metabolism resulting in PKM1 compensating for the loss of PKM2 further emphasising the importance of both isoforms in the context of abnormal cell proliferation [21,22].

Cells uptake glucose by facilitated diffusion through Glut transporters. Many cancers upregulate different members of the Glut gene family to provide increased glucose supply and glycolytic flux [23,24]. One of the mechanisms inhibiting glucose uptake to restore glucose homeostasis is endocytic internalisation of Glut receptors stimulated by several members of the alpha-arrestin family of proteins. Thioredoxin-interacting protein (TXNIP) and arrestin-4 (ARRDC4) are the most studied members of the alpha-arrestin family [25–28]. TXNIP and ARRDC4 are close homologues and show over 40% identity in amino acid sequence [27,29]. Both the TXNIP and ARRDC4 genes are upregulated in response to glucose stimulation by the binding of heterodimeric MondoA/B:MLX transcription factors to a common regulatory sequence, the double-E-box-like promoter element known as the carbohydrate-response element (ChoRE), within their promoters [30–35].

TXNIP was originally identified as vitamin D3 upregulated protein 1 (VDUP1) in HL60 cells and was later shown to bind the reduced thioredoxin (TXN) via a disulphide bond involving Cys247 of TXNIP and hence to constitute a negative regulator of the thioredoxin antioxidative system [32,36–38]. In recent years, redox-dependent and -independent functions of TXNIP made it a key player in the pathogenesis of many metabolic, cardiovascular and neurodegenerative disorders [39–42]. Due to its proapoptotic, proinflammatory and antiproliferative function, TXNIP is an important tumour suppressor gene, commonly silenced in various cancer cells [43–45].

Here, we decided to systematically characterise the transcriptional, epigenetic and metabolic effects of depletion of PK, since this enzyme (i) has been shown to be the key rate-limiting enzyme in aerobic glycolysis, (ii) has been proposed to be a potential anti-cancer target and (iii) can play a pro-tumorigenic role beyond glycolysis by functioning as a transcription factor [6,11,15,21,46,47]. We show that suppression of PK activity by a stable knockdown of PKM1/2 in immortalised, fast-proliferating human cell lines leads to the accumulation of glucose-6-phosphate (G6P) and MondoA:MLX-mediated upregulation of TXNIP. Further, we suggest that this new regulatory axis is not limited to cancer cell lines but also present in various metabolically relevant models including mouse primary hepatocytes and zebrafish embryos. By investigating redox-dependent function of TXNIP, we propose that the metabolism-driven upregulation of TXNIP could lead to the increased production of reactive oxygen species and, subsequently, increase in oxidative damage to DNA and other cellular structures. Altogether, our findings advance our understanding of the metabolic perturbances associated with abnormal activity of PK.

2. MATERIAL AND METHODS

2.1. Cell culture

HEK293 and MCF-7 cell lines were cultured in DMEM (HEK293 and MCF-7 with 1 g glucose/L, HEK293T with 4.5 g glucose/L) supplemented with 10% FBS (Gibco), 2 mM L-glutamine, 1% Pen/Strep, 1 mM sodium pyruvate and non-essential amino acids and maintained at 37 °C.

Drosophila Schneider 2 cells were cultured at 27 °C, in Schneider medium (Thermo Fisher) supplemented with 10% heat-inactivated FBS (Gibco) and 0.5% Pen/Strep.

2.1.1. Stable knockdown generation

Stable knockdown in HEK293 and MCF-7 cells was generated using lentiviral-delivered shRNA. Lentiviral vector particles were produced by HEK293T cells transfected with shRNA inserted into pLKO.1-puro plasmid (Addgene #8453) using LENTI-Smart kit (Invivogen) and secreted into cell culture medium. Lentiviral particles were collected at 14–18 h and 48 h after transfection, centrifuged at 2000 rpm for 5 min, filtered through 0.45 μm PVDF syringe filter and immediately used. Target cells were incubated with lentiviral particles and 8 μg/mL hexadimethrine bromide (Sigma) for 14–18 h. After transduction, fresh medium was added for 24 h before selection medium with 2.5 μg/mL puromycin was applied. Every batch of knockdown cells was afterwards validated by RT-qPCR.

2.1.2. siRNA transfection of HepaRG cells

Before transfection, HepaRG cells were differentiated into hepatocyte- and cholangiocyte-like cells for four weeks by cultivation in William's E medium (Invitrogen) supplemented with 10% FBS Fetaclone II (HyClone), 1% Pen/Strep, 2 mM L-Glutamine, 0.023 IE/mL human insulin (Sanofi Aventis), 4.7 μg/mL hydrocortisone (Pfizer) and 80 μg/mL gentamicin (Ratiopharm) with medium exchange twice weekly. After two weeks, DMSO (Sigma) was added to a final concentration of 1.8%.

After differentiation, cells were transfected with 10 μM control or PKM or PKLR siRNA (SMARTPool, Dharmacon; control siRNA was non-targeting siRNA designed and microarray tested by the supplier for minimal targeting of human, mouse or rat genes) or a combination of both using Lipofectamine RNAiMAX (Thermo Fisher) according to manufacturer's instruction on day 1 and 4, and harvested on day 7. RNA extraction was performed using Quick-RNA Miniprep Kit (Zymo Research).

2.1.3. siRNA transfection of murine hepatocytes

Primary murine hepatocytes from 8 to 12-weeks-old C57BL6/N mice (Janvier Labs) were isolated using collagenase perfusion [48,49]. 2×10^5 cells per well were seeded in collagen-coated (Sigma–Aldrich) 24-well plates (Thermo Fisher Scientific). Hepatocytes were cultured in William's Medium E (PAN-Biotech) containing 10% FCS (PAN-Biotech), 5% Pen/Strep (Thermo Fisher Scientific) and 100 nM dexamethasone (Sigma–Aldrich) and maintained at 37 °C and 5% CO_2 for 1 h. Next, cells were washed with PBS (Thermo Fisher Scientific) and incubated with 80 nM Pklr or control siRNA (SMARTPool,

Dharmacon; control siRNA was non-targeting siRNA designed and microarray tested by the supplier for minimal targeting of human, mouse or rat genes) and interferin (1.2 μL/well) (Polyplus) for 6 h until a second layer of collagen was added to maintain the cells in sandwich culture [49] in William's Medium E medium containing 10% FCS, 5% Pen/Strep. Medium was changed every second day.
Cells were harvested for RNA isolation 3 days after induction of RNAi by washing once with ice-cold PBS before adding RNA Lysis Buffer (Zymo Research). RNA extraction was performed using Quick-RNA Miniprep Kit (Zymo Research) according to manufacturer's instruction.

2.1.4. Extracellular acidification rate (ECAR) measurements

One day before the assay, the cells were seeded on the Seahorse XF96 cell culture microplate at the density 2×10^4 cells per well in 15 replicates, incubated for 1 h at room temperature and further overnight at 37 °C. On the day of the assay, the cells were washed twice with the assay medium (Seahorse XF Base Medium without phenol red, supplemented with 10 mM glucose and 2 mM L-Glutamine) and incubated at 37 °C without CO_2 supply for 1 h. The assay was performed using Seahorse XF96 Analyzer (Agilent). After the assay initialisation and establishing the baseline, 3 sequential injections of glucose (Sigma, final concentration 10 mM), oligomycin (Sigma, final concentration 3 μM) and 2-deoxyglucose (Sigma, final concentration 100 mM) were performed. After every injection the plate was subjected to 3–5 cycles of mixing (3 min) and measurement (3 min).

2.1.5. Transient transfection and MTT assay

Cells were transfected with plasmids encoding variants of TXNIP or control vector using Lipofectamine 3000 (Thermo Fisher) according to manufacturer's instructions. Two days after transfection, thiazolyl blue tetrazolium bromide solution (Sigma) was added to the medium to the final concentration of 0.45 mg/mL and incubated at 37 °C for 3 h. After the incubation, the medium was gently aspirated and the formazan crystals were dissolved by gentle rocking with 500 μL DMSO for 2 h, protected from light. Absorbance of the solution at 570 nm and 690 nm (background) was measured using the microplate reader.

2.2. Zebrafish strains and care

Zebrafish were kept at 26 °C in a recirculating water system and were staged according to [50]. Mutant offspring was obtained by natural spawning from incrosses of homozygous pkma2/pkmb/myl7:eGFP and are referred to as pkma/b −/− throughout the manuscript. AB was used as a wildtype control.
The following alleles were used: pkma: pkma2^{s717} [51]; pkmb: pkmb^{s718} [51]; myl:eGFP: Tg (myl7:EGFP-Hsa.HRAS) [52].

2.3. Chromatin immunoprecipitation (ChIP)

2.3.1. Preparation of chromatin from human cells

Adherent human cell lines were crosslinked for 5 min at room temperature with 1% formaldehyde (Sigma) and quenched with 125 mM glycine (Sigma). The cells were washed 3 times with ice-cold PBS supplemented with cOmplete Protease Inhibitor cocktail (Roche), 10 mM sodium butyrate (NaBu, Alfa Aesar) and 10 mM NAM (Roth), scraped, pelleted, resuspended in lysis buffer (50 mM Tris pH 8.0, 2 mM EDTA, 0.1% IGEPAL, 10% glycerol, 10 mM NaBu, 10 mM NAM, 1× PIC) and incubated for 5 min. The suspension was pelleted and resuspended in shearing buffer (50 mM Tris pH 8.0, 10 mM EDTA, 1% SDS, 10 mM NaBu, 10 mM NAM, 1× PIC). Chromatin was sonicated for 5 min at 80% amplitude using QSonica Q800R. A fraction of sonicated chromatin was mixed with RNase A (Thermo Fisher) and proteinase K (Roche), de-crosslinked overnight at 65C and purified using QIAquick PCR purification kit. DNA concentration was measured using Varioskan LUX (Thermo Fisher).

2.3.2. Preparation of chromatin from *Drosophila* cells

Drosophila S2 cells were crosslinked for 5 min at room temperature with 1% formaldehyde (Sigma) and quenched with 125 mM glycine (Sigma). The cells were washed 3 times with ice-cold PBS, resuspended in ice-cold IP buffer (50 mM Tris pH 7.5, 150 mM NaCl, 5 mM EDTA, 0.5% IGEPAL, 1% Triton X-100, 10 mM NaBu, 10 mM NAM, 1× PIC), incubated for 10 min and pulled through the syringe with a 27G needle. The cells were pelleted and the homogenisation cycle was repeated. The pellet was resuspended in shearing buffer and sonicated for 13 min 20 s at 80% amplitude using QSonica Q800R. From this point *Drosophila* chromatin was treated like described in 2.3.1.

2.3.3. Immunoprecipitation

Chromatin was diluted 10 times with ChIP dilution buffer (50 mM Tris pH 8.0, 200 mM NaCl, 0.5% IGEPAL). Before IP, chromatin samples were pre-cleared with sepharose beads coupled to protein A and protein G (A/G beads, GE Healthcare) and blocked with BSA (NEB) and tRNA from *S. cerevisiae* (Sigma). The pre-cleared chromatin was mixed with relevant antibodies (H3K9ac: Abcam ab4441, H3K4me3: Millipore 17–614, MLXIP: Proteintech 13614-1-AP, MLX: Cell Signalling #85570) and incubated overnight at 4 °C with rotation. Next, 40 μL of pre-blocked A/G beads were added and incubated for 2 h. The samples were washed with low salt- (150 mM), high salt- (500 mM) and TE buffer (2 washes each) and eluted with 100 mM $NaHCO_3$ with 1% SDS for 30 min at 30 °C with shaking. Eluted samples were de-crosslinked as described in 2.3.1. De-crosslinked samples were used for qPCR (Supplementary data file 1) or for NGS analysis. Each IP variant was performed in 2 replicates, unless stated otherwise.

2.3.4. DNA library preparation

DNA library was prepared using NEBNext Ultra II DNA Library Prep Kit, NEBNext Multiplex Oligos for Illumina and AMPure XP beads (Beckman Coulter) according to the manufacturer's instructions. The size distribution of obtained DNA fragments was checked using Bioanalyzer 1000 or Bioanalyzer High Sensitivity Chip (Agilent). For details on data analysis see Supplementary data file 2.

2.4. Immunoblotting

Proteins were extracted using RIPA buffer, then separated by SDS-PAGE and transferred to the nitrocellulose membrane. The membrane was blocked with 5% nonfat-dried milk in TBST and incubated with the relevant primary (PKM1: Cell Signaling #7067, PKM2: Cell Siganling #4053, ACTB: Cell Signaling #4967, TXNIP: Cell Signaling #14715, TUBA1B: Abcam ab6160) and HRP-conjugated secondary antibody (anti-rabbit: Jackson ImmunoResearch 211-032-171, anti-rat: Jackson ImmunoResearch 712-035-150, anti-mouse: Dako P0447). The signal was developed using Clarity Western ECL Substrate (Bio-Rad).

2.5. RNA analysis

2.5.1. RT-qPCR

Total RNA from mammalian cells was extracted using Quick-RNA Miniprep Kit (Zymo Research) and from zebrafish embryos using RNeasy Mini Kit (Qiagen) with modifications. 0.3–1.0 μg total RNA was reverse transcribed using RevertAid First Strand cDNA Synthesis Kit (Thermo Fisher).1 μL cDNA was used as a template in the qPCR

reaction together with 1× Absolute Blue qPCR Sybr Green (Thermo Fisher) and 100 nM forward/reverse reverse primer mix (Supplementary data file 1). The reaction was performed in a LightCycler 96 system (Roche). The RNA abundance was normalized to the beta-2-microglobulin (B2M) gene.

2.5.2. RNA-seq

Control and PKM knockdown cells were thawed and cultured in parallel, the number of passages was similar yet not equal, due to the longer generation time of the PKM knockdown in HEK293 model. Before harvesting the cells, fresh medium was added for 12–16 h. Total RNA was extracted using Quick-RNA Miniprep Kit (Zymo Research). RNA concentration was measured using Qubit RNA BR Assay Kit (Thermo Fisher) and RNA integrity was monitored by Bioanalyzer 6000 Nano Chip (Agilent). RNA library was prepared using standard NEBNext RNA Library Prep Kit for Illumina (NEB) and submitted for sequencing with approx. 35×10^6 paired-end reads per library.

Residual adapter sequences and low-quality segments were trimmed out of the RNA-seq reads were using Trim Galore [53]. Resulting sequences were quantified against the hg38 transcriptome index from refgenie (hg38/salmon_sa_index) [54] using Salmon [55] with the following settings: –seqBias –gcBias —validateMappings.

A differential expression analysis between WT and KD samples has been performed using DESeq2 [56], with local fit for dispersion estimates and dispersion outlier filtering disabled. Only genes that had at least 10 reads mapped to them in all samples were considered. Resulting differentially expressed genes (Wald test, FDR 0.05) have been divided into categories based on their confident effect sizes [57]. MCF-7 and HEK293 datasets were analysed independently.

2.6. 13C-glucose labelling

For 13C-glucose labelling, HEK293 cells were grown in glucose-free DMEM (Gibco) supplemented with 1 g/L D-Glucose-$^{13}C_6$ (Sigma), 10% FBS (Gibco), 2 mM L-Glutamine, 1% Pen/Strep 1 mM sodium pyruvate and non-essential amino acids. After 5 h of labelling, the medium was aspirated, the cells were placed on ice, washed twice with ice-cold PBS, scraped from the dish and transferred to the pre-cooled low-bind 1.5 mL tube. The cells were centrifuged for 3 min at 300 × *g*, 4 °C, and after removing the residual PBS immediately snap frozen in liquid nitrogen.

2.7. Metabolomic analysis

2.7.1. Metabolites extraction

Metabolites were extracted from frozen pellets with 300 μL of cold mix methanol:water (8:1/v:v) with internal standard (d3-Leucine at 5ppm). Cell lysis was carried out with three rounds of freeze and defrost by liquid N_2 immersion and sonication, followed by 1 h in ice before centrifugation (12,000 rpm, 10 min at 4 °C).

2.7.2. GC–MS settings

270 μL of extract were dried under a stream of N_2 gas and lyophilized before chemical derivatization with 40 μL methoxyamine in pyridine (40 μg/μL) for 45 min at 60 °C. Samples were also silylated using 25 μL N-methyl-N-trimethylsilyltrifluoroacetamide with 1% trimethylchlorosilane (Thermo Fisher Scientific) for 30 min at 60 °C to increase volatility of metabolites. A Thermo Scientific™ TRACE™ 1310 GC system coupled to an Exactive GC Orbitrap mass spectrometer (Thermo Scientific, Waltham, MA) was used for isotopologue determination. Derivatized samples were injected (1 μL) in the gas chromatograph system using a split ratio of 5 with HP-5MS chromatographic column (30 m length × 0.25 mm i. d., 0.25 μm film thickness, Agilent Technologies). Helium (99.999% purity) was used as a carrier gas at a flow rate of 1.5 mL/min. The GC oven program started with an initial temperature of 70 °C, followed by a ramp of 11 °C/min to 190 °C, then to 325 °C at 21 °C/min, and finally held at this temperature until a total run time of 20 min. Metabolites were ionized using positive chemical ionization (CI) with isobutane as reagent gas with a flow at 0.7 mL/min. The ion source and the transfer line temperatures were 200 and 280 °C, respectively. The instrument operated at a resolution of 60,000 (FWHM *m/z* 200) and the automatic gain control (AGC) target was set to 1 × 106. The MS data were acquired in full-scan mode covering a mass range from 60 to 800 *m/z*.

2.7.3. Data processing and statistical analysis

Raw data was transformed into mzML open format in order to process it with isoSCAN R package [58]. Using isoSCAN the following were performed: targeted isotopologue quantification, C13 natural abundance subtraction, fractional contribution (FrC) calculation and normalization using d3-Leucine. isoSCAN quantification parameters (peak width, SNR and scan counts) were optimized to avoid noise and maximize signal quantification, these were contrasted by manually evaluation of the raw data.

2.8. ROS quantification

Cells after defined treatment were collected from the plates by trypsinisation, resuspended in full medium supplemented with 10 uM DCFDA (Abcam) and incubated for 30 min at 37 °C, protected from light. After the incubation, the cells were centrifuged and resuspended in 1 mL PBS. The cells were passed through the 0.4 μm strainer and 7-AAD (Miltenyi) was added to the cell suspension to the final concentration 0.525 μg/mL. The cells were incubated on ice for 10 min and the fluorescence signal was measured using CytoFLEX flow cytometer (Beckman Coulter). The data was analysed using CytExpert (Beckman Coulter) and floreada.io online software.

2.9. Quantification of 8-oxo-dG in genomic DNA

Genomic DNA was extracted using Quick-DNA Miniprep Kit (Zymo Research). Derivatisation of genomic DNA and LC-MS/MS analysis was performed as described in [59]. Briefly, DNA was spiked with heavy-labelled nucleosides and digested with Nucleoside Digestion Mix (NEB). The samples were filtered through an AcroPrep Advance 96 filter plate 0.2 μm Supor (Pall Life Sciences) before applying to LC-MS/MS.

The LC-MS/MS analysis was performed using an UHPLC-QQQ-MS/MS system consisting of a Triple Quadrupole 6490 mass spectrometer (Agilent) with an ESI source and an Agilent Infinity 1290 UHPLC. The elution was monitored at 260 nm (Agilent InfinityLab Deuterium Lamp G1314). Nucleosides were separated on an InfinityLab Poroshell 120 SB-C8 column (2.1 mm × 150 mm, 2.7 μm, Agilent Technologies, USA) at 35 °C with the parameters and conditions as described in [59]. Data Acquisition and processing were performed using MassHunter Workstation Software Version B.07.01 (Agilent).

3. RESULTS

3.1. Knockdown of PKM drives TXNIP expression

Alterations of nutrient availability, including glucose, can lead to pronounced transcriptional and epigenetic changes in multiple organisms [60–63]. However, how depletion of a key rate-limiting enzyme in glycolysis, PK (Figure 1A) impacts on both transcriptional and

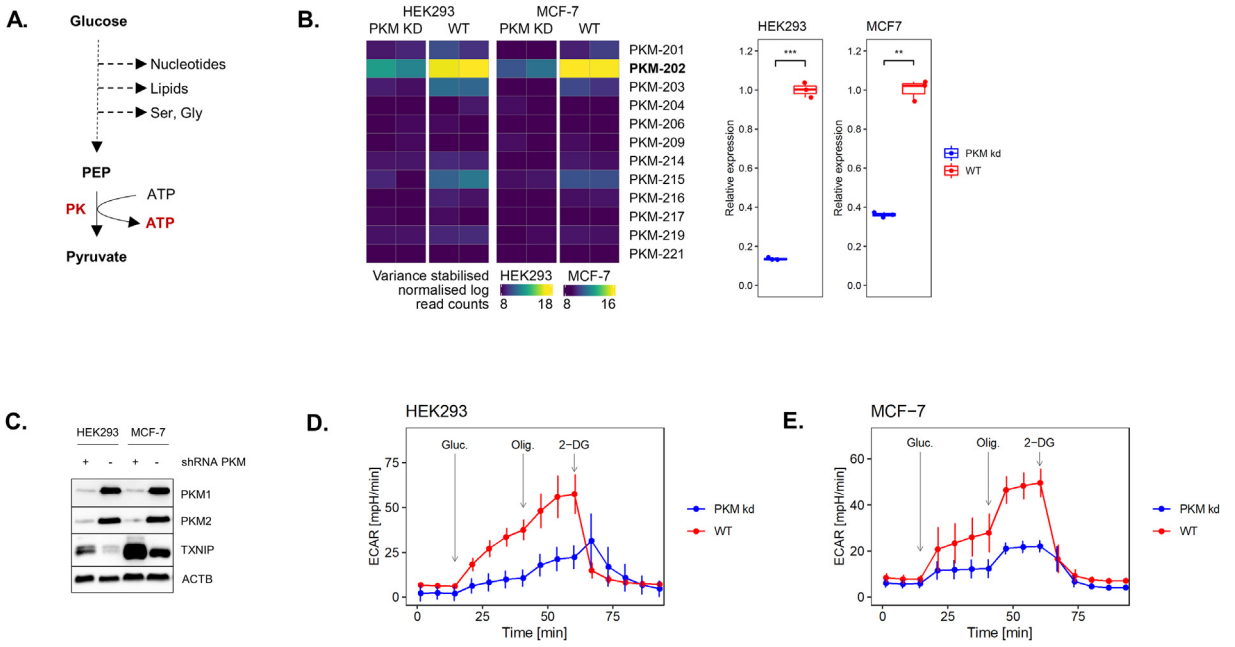

Figure 1: Knockdown of PK impairs glycolysis. (A) Simplified scheme of the glycolytic pathway with the reaction catalysed by PK indicated in red. (B) Heatmap showing the abundance of protein-coding PKM transcripts; Data derived from our RNA-seq. The most abundant isoform encoding PKM2 (PKM-202) is indicated in bold (left) and RT-qPCR quantification of a common fragment of all PKM transcripts; n = 3, Student's t-test, $^{**}p < 0.01$, $^{***}p < 0.001$ (right) upon stable shRNA-mediated PKM knockdown and wild type (WT) HEK293 and MCF-7 cells. (C) Representative immunoblot of total protein extracts from HEK293 and MCF-7 cells upon stable PKM knockdown with the indicated antibodies. (D, E) Extracellular acidification rate (ECAR) measurements obtained with HEK293 (D) and MCF-7 (E) cells over time using extracellular flux analyser. Difference in glycolytic-derived lactate production was tested by sequential addition of glycolysis inducer glucose (Gluc.), ATP synthase inhibitor oligomycin (Olig.) and early glycolysis inhibitor 2-deoxyglucose (2-DG); Each datapoint shows the average value of 15 replicates ± SD.

epigenetic pathways is currently unclear. To determine transcriptional and histone modification changes upon induced depletion of PK activity in highly glycolytic cells, we established a stable PKM knockdown in human embryonic kidney 293 (HEK293) and in Michigan Cancer Foundation-7 (MCF-7) cell lines using shRNA targeting a common fragment of the spliced PKM1/2 transcript [64,65]. We confirmed the efficiency of the knockdowns of both isoforms at the level of mRNA and protein by RT-qPCR, RNA-seq and immunoblotting (Figure 1B—C). As expected, we observed the most pronounced reduction of the transcript PKM-202 encoding isoform PKM2, which is most abundant in fast-proliferating cells [66]. PKM-depleted HEK293 cells displayed increased doubling time and altered cellular morphology, similar to the changes observed by Wang et al. upon treatment of cells with shikonin, non-specific PKM2 inhibitor [67]. Next, to validate our models, we determined if our knockdown cell lines indeed display reduced glycolytic activity. For this, we induced glycolysis after 1 h of glucose starvation, by injection of glucose to the culture medium and monitored extracellular acidification rate (ECAR) in live cells. As shown in Figure 1D—E, the amount of released glycolysis-derived lactate was significantly lower upon PKM depletion and this effect was further augmented by oligomycin. Inhibition of the initial reaction of glycolysis by 2-deoxyglucose (2-DG) did not result in different non-glycolytic acidification rates between wild-type and knockdown cells confirming that our PKM knockdown reduced the functionality of glycolysis.

Having validated that our stable knockdown impairs glycolysis, we investigated how the altered metabolic state due to PKM depletion impacts gene expression. In order to identify the genes affected by PKM depletion, we performed RNA sequencing on wild-type and PKM knockdown HEK293 and MCF-7 cells. DESeq2 differential enrichment analysis [56] identified 527 and 2015 additional genes misregulated (FDR = 0.05) in HEK293 and MCF-7 respectively (Figure 2A).

To compare the expression changes across both cell lines, we next calculated and correlated the confident $\log_2$ fold expression changes [57] (Figure 2B). This analysis showed that 111 genes were consistently downregulated in both HEK293 and MCF-7 cells, of which only five genes (CBFB, GEMIN2, PKM, PPT1, VTI1B) were downregulated in both cell lines with a confident log2 fold change of −0.5 or lower. Additionally, 24 genes were upregulated in both cell lines, out of which only TXNIP was upregulated at the highest confidence level in both HEK293 and MCF7. By performing transient siRNA-mediated knockdown of PKM in HEK293 and MCF-7 cells, we confirmed that the upregulation of TXNIP is a specific response to PKM depletion (Supplementary Fig. 1).

As PKM knockdown can affect the levels of epigenetically relevant metabolites, we reasoned that a change in the global landscape of histone modifications could cause the observed changes in gene expression. Thus, we performed chromatin immunoprecipitation (in HEK293 cells) with a reference exogenous genome (ChIP-Rx) as a spike-in control for normalisation for H3K9ac and H3K4me3, two histone modifications linked to active transcription [68] (Supplementary data file 2). Interestingly, our analysis did not detect a major reprogramming of the global H3K9ac and H3K4me3 chromatin landscape upon PKM knockdown (Figure 2C—D and Supplementary Fig. 2). We rather observed a gain of H3K9ac and H3K4me3 signal at peaks overlapping with promoters of upregulated genes which correlated with the level of transcriptional increase (Figure 2E—F). Notably, TXNIP, which gained the most substantial amount of H3K4me3 and H3K9ac at its promoter, was also the most highly

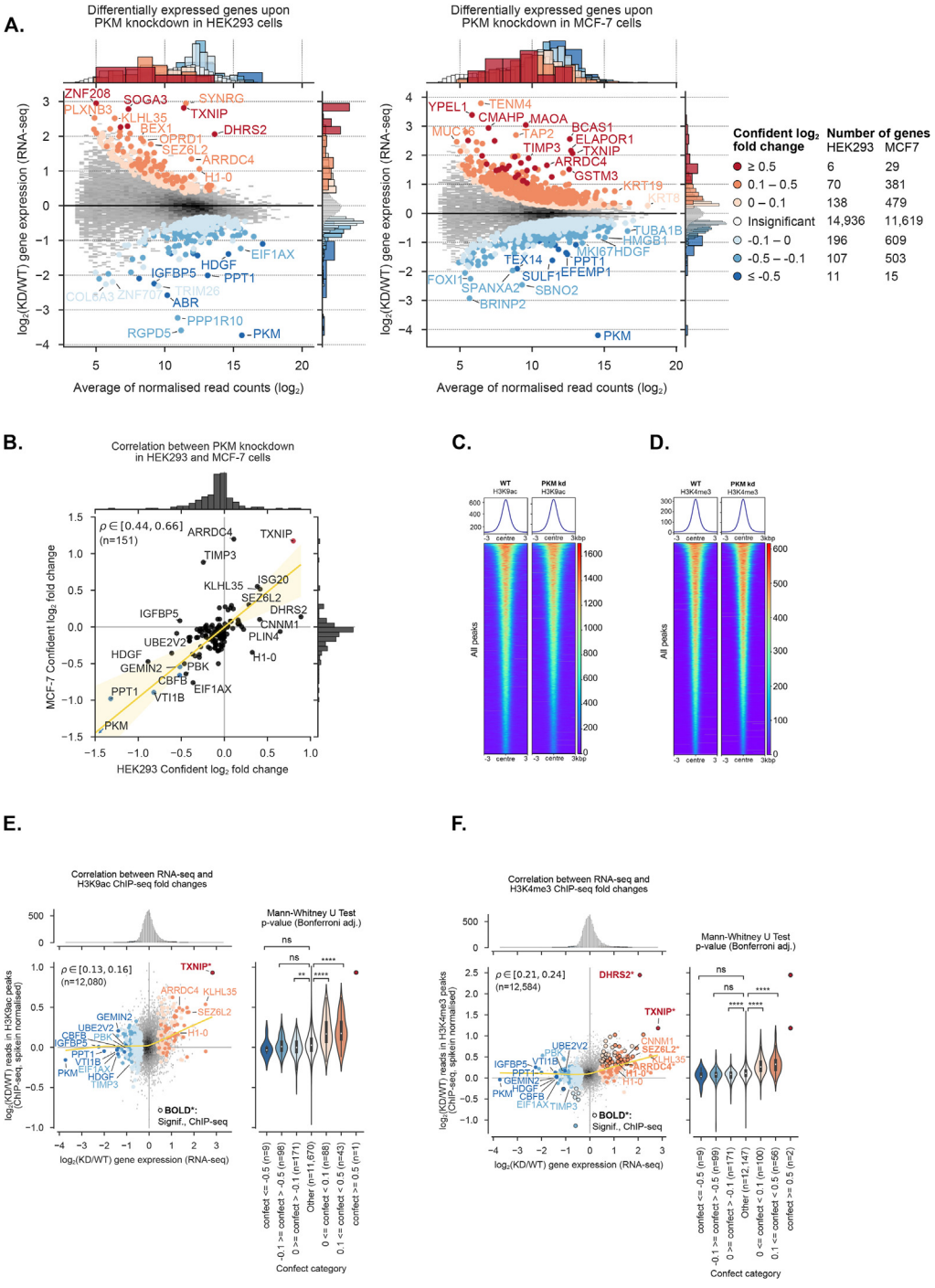

Figure 2: Impact of PKM knockdown on the transcriptome and epigenome of HEK293 and MCF-7 cells. (A) Log ratio-mean expression (MA) plot, with differentially expressed genes marked and colour-coded according to their confident log2 fold change upon stable knockdown in HEK293 (left) and MCF-7 (right). Number of genes in each category is displayed in the table on the right. (B) Correlation of confident log2 fold changes upon stable PKM knockdown between HEK293 (x-axis) and MCF-7 (y-axis) cell lines. The 95% confidence interval (CI) for spearman correlation coefficient (ρ) estimate is displayed in the top-left corner, and the linear regression line shown in yellow. Genes down- and up-regulated with a confident log2 fold change of at least 0.5 are highlighted in blue and red respectively. Only genes with a confident log2 fold change estimate in both experiments are shown. Datapoint for PKM is beyond the axes range. (C, D) Heatmaps and profile plots comparing the normalised read counts of H3K9ac (C) and H3K4me3 (D) ChIP-Rx in WT and PKM knockdown cells over the consensus peak set for each target. The regions are centered at the middle of the peak and extended by 3 kbp up- and downstream. The color indicates the read counts in peaks. Data from representative replicate (see also Supplementary Fig. 2 for second replicate). (E, F) Correlation between the log2 fold change in gene expression (RNA-seq, x-axis) and ChIP-Rx normalized signal levels at their promoter-overlapping peaks (y-axis) for H3K9ac (E) and H3K4me3 (F) ChIP experiments. The overall trend is indicated by the yellow lowess line. 95% CI for Spearman ρ is indicated in the top-left corner. The genes are divided into categories based on their confident log2 fold change as in (A), marginal distributions and their statistical differences are displayed on the right: Mann–Whitney U test, Bonferroni adjusted: ns $p > 0.05$, *$p \leq 0.05$, **$p \leq 0.01$, ***$p \leq 0.001$, ****$p \leq 0.0001$. The genes labeled in (B) are also indicated here. The datapoints with darker border and bolded labels with an asterisk highlight the peaks with statistically significant changes in ChIP-Rx read abundance (DESeq2, FDR <0.1, see Supplementary data file 2 for details).

upregulated gene in both cell lines. This suggests that PKM levels could contribute to the regulation of TXNIP expression by controlling the histone modification signature at the promoter.

3.2. Knockdown of PKM impairs glycolytic flux and leads to the accumulation of glucose-6-phosphate

The results of the differential gene expression analysis prompted us to study the impact of PK depletion on cellular metabolism in more detail. As reported in multiple previous studies [30,31,33,69], in response to elevated glucose-6-phosphate (G6P) levels, the heterodimeric transcription factor MondoA/B:MLX binds two double E-box carbohydrate response elements (ChoREs) present both in the promoter of both TXNIP and ARRDC4, to drive their expression. To investigate whether depletion of PKM activity results in the accumulation of glycolytic intermediates, such as G6P, and changes in glycolytic flux that could be implicated in TXNIP activation, we applied stable isotope labelling with 13C-glucose and quantified the amount of glycolytic metabolites.

From the 10 glycolytic intermediates upstream of PKM, we were able to detect 8 metabolites (Figure 3A). Among these, the total abundances of 6 metabolites were significantly elevated in PKM knockdown cells (Figure 3B). For the remaining two, the levels of fructose-6-phosphate showed the same trend without reaching statistical significance. The levels of free glucose, that upon entering the cell is immediately phosphorylated by hexokinase, were not altered. To investigate whether the increased abundance of glycolytic intermediates was caused by the altered flux through this pathway, we analysed the fraction of 13C-labelled G6P in knockdown and WT cells. We observed that after 5 h of 13C-labelling, in WT cells 100% of G6P was derived from 13C-labelled glucose in contrast to only 70% in PKM knockdown cells, suggesting that slower conversion of G6P due to a reduced metabolic flux is the cause of its accumulation upon PKM knockdown (Figure 3C).

When glycolytic metabolites are in excess, they can be shunted towards the branching pathways [70,71]. We therefore also measured the total abundances and 13C-enrichment of serine (Ser) and ribose-5-phosphate (R5P) — end products of serine synthesis and pentose phosphate pathways, respectively. As expected, we found that in PKM knockdown cells, the levels of both Ser and R5P were increased and the contributions of both 13C-labelled isotopologues was higher than in WT cells (Figure 3D—E). Altogether these results reveal an accumulation of the glycolytic intermediate G6P upon PKM depletion, what subsequently results in shunting of metabolites towards branching pathways.

3.3. Knockdown of PKM activates MondoA:MLX transcription factors

The increased G6P levels prompted us to investigate the role of MondoA/B:MLX in the upregulation of TXNIP and ARRDC4 upon PKM knockdown. For this, we first performed ChIP followed by qPCR analysis in order to determine the binding of the transcription factors to the TXNIP and ARRDC4 ChoREs. We decided to focus on MLX and MondoA since our RNA-seq analysis showed that expression level of MondoB is lower than MondoA in both cell lines. While the mRNA levels for all these transcription factors were not majorly altered upon PKM knockdown (only MLX shows a slight downregulation in MCF-7 in the analysis with the lowest confect threshold), we observed significant enrichment of MondoA and MLX occupancy at the ChoREs of both TXNIP and ARRDC4 (Figure 4A—B). Next, we performed ChIP-seq for MondoA and MLX to complement this with

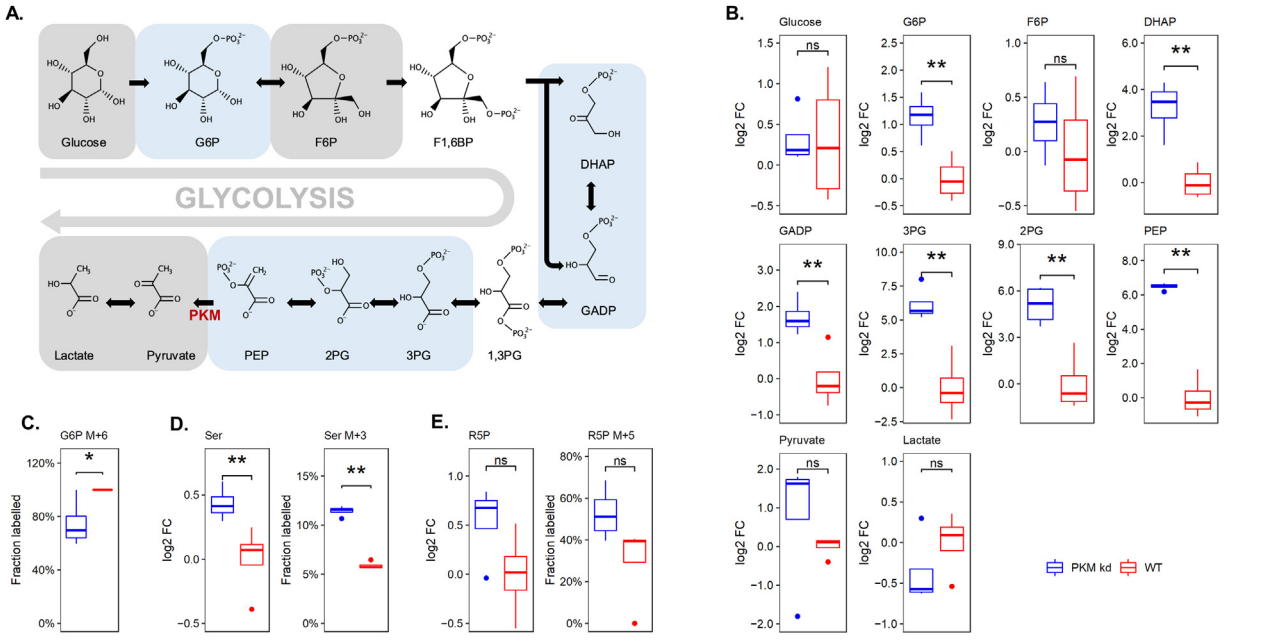

Figure 3: Knockdown of PKM impairs flux of metabolites in glycolysis and branching pathways. (A) Scheme of the glycolytic pathway and its intermediate metabolites. Compounds detected in the metabolomic analysis are indicated by the shaded background (in blue — elevated upon PKM knockdown, in grey — not significantly changed upon PKM knockdown; Student's t-test, $p < 0.05$). (B) Log2 fold change of the abundance of detected glycolytic metabolites between PKM knockdown and WT HEK293 cells. (C) Fraction of 13C-labelled G6P after 5 h of 13C-glucose labelling. (D) Log2 fold change of abundance of total Ser (left) and fraction of 13C-labelled Ser (right) after 5 h of glucose labelling. (E) Log2 fold change of abundance of total R5P (left) and fraction of 13C-labelled R5P (right) after 5 h of 13C-glucose labelling. $n = 4$, Student's t-test, ns $p \geq 0.05$, *$p < 0.05$, **$p < 0.01$, p values in (B) adjusted with BH method; 1,3-PG — 1,3-bisphospoglyceate, 2 PG — 2-phosphoglycerate, 3 PG — 3-phosphoglycerate, DHAP — dihydroxyacetone phosphate, F1,6BP — fructose-1,6-bisphosphate, F6P — fructose-6-phosphate, G6P — glucose-6-phosphate, GADP — glyceraldehyde-3-phosphate, PEP — phosphoenolpyruvate, R5P — ribose-5-phosphate, Ser — serine.

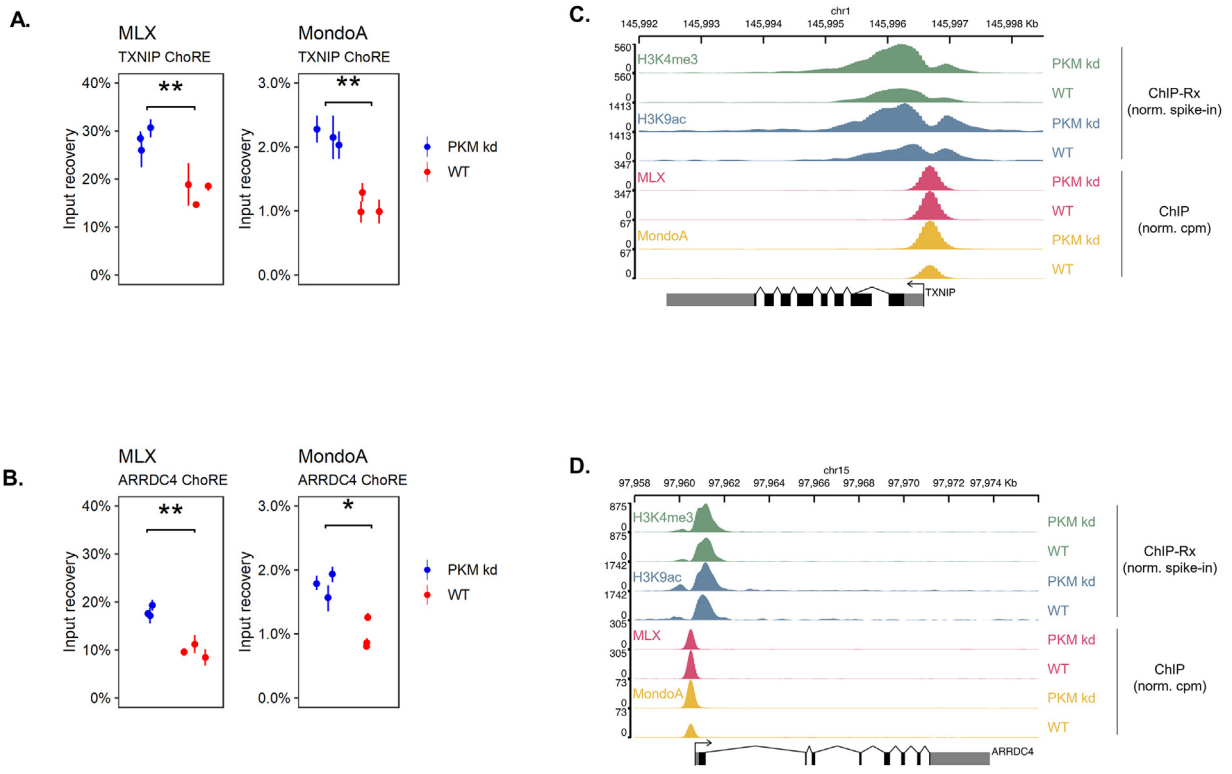

Figure 4: Changes of chromatin signatures at the promoters of TXNIP and ARRDC4 upon knockdown of PKM in HEK293 cells. (A, B) ChIP-qPCR analysis of MLX (left) and MondoA (right) enrichment in carbohydrate-response elements (ChoREs) of TXNIP (A) and ARRDC4 genes (B); Each data point represents an average qPCR value ± SD of an independent IP sample; n = 3, Student's t-test, *p < 0.05, **p < 0.01. (C, D) Genome browser tracks showing read densities for the indicated histone PTMs and TFs at the promoter region of TXNIP (C) and ARRDC4 (D). Gene schemes and orientations are shown at the bottom, genomic locations and scale at the top. ChIP-seq reads of histone PTMs were normalised using Drosophila spike in (ChIP-Rx), ChIP-seq reads of TFs were cpm normalised (see also Supplementary data file 2 for more details).

genome-wide information about their binding profiles. For MLX we detected a very limited number of peaks of which the ones with the highest signal intensity mapped close to the TXNIP and ARRDC4 genes (Figure 4C–D). This confirms our qPCR results of MLX binding. However due to the small total number of detected peaks, we were not able to perform differential enrichment analysis comparing WT and PKM knockdown samples. Our MondoA ChIP-seq detected enough binding sites to determine differential binding. Interestingly, only the promoter regions of TXNIP and ARRDC4 showed a clear gain of MondoA signal after the knockdown (Figure 4C–D) which is in line with our qPCR results.
Together, this suggests that PKM knockdown results in the accumulation of intracellular G6P leading to increased occupancy of MondoA and MLX specifically at the TXNIP and ARRDC4 promoters. Thus, the PKM/MondoA/MLX axis is a major regulator of a small set of specific genes and PKM can act via G6P as fine tuner of global transcriptional profiles.

3.4. TXNIP upregulation triggers ROS accumulation and induces oxidative damage to DNA

TXNIP is a ubiquitously expressed protein with (i) a unique role to negatively regulate thioredoxin function, and (ii) alpha arrestin-associated role to control a broad range of cellular energy metabolism [28,32,44]. A major function of various alpha-arrestins is inhibition of glucose uptake what can lead to the inhibition of cell proliferation [72,73]. To investigate how the redox-specific function of upregulated TXNIP affects the phenotype of HEK293 cells, we generated constructs for the overexpression of redox-active TXNIP (TXNIP WT) and a TXNIP mutant with the cysteine residue at position 247 replaced by serine (TXNIP C247S) rendering TXNIP devoid of its redox-specific function [29]. Immunoblotting confirmed that both variants of TXNIP were comparably expressed upon overexpression in HEK293 cells (Figure 5A). As expected, our MTT assays showed that overexpression of TXNIP reduced metabolic activity (Figure 5B). Interestingly, the C247S mutation partially rescued this effect. Thus, it is possible that the redox-dependent function of TXNIP could contribute to the reduced proliferation we observed. Next, to investigate if a higher level of reactive oxygen species (ROS) could contribute to reduced cell proliferation upon TXNIP overexpression, we quantified the abundance of a DCFDA probe that becomes fluorescent upon oxidation to DCF by various cellular ROS, in the cells overexpressing different TXNIP variants. As displayed in Figure 5C and quantified in Supplementary data file 3, we detected elevated level of ROS in the cells overexpressing TXNIP WT, while the signal from cells expressing TXNIP C247S was comparable to the negative control. Overall, these results suggest that overexpression of TXNIP WT leads to the increased ROS production and might be linked to inhibition of cell proliferation. While our assays control for the effects of general TXNIP protein toxicity, we cannot rule out cellular toxicity effects specific for TXNIP WT that could provide alternative explanations for the observed phenotypes.
To complement our transient overexpression results where TXNIP protein levels are higher than upon physiological upregulation by MondoA:MLX, next we wanted to determine ROS level upon PKM knockdown. For this we used mass spectrometry to quantify the amounts of DNA oxidation marker 8-oxo-2′-deoxyguanosine (8-oxo-dG)

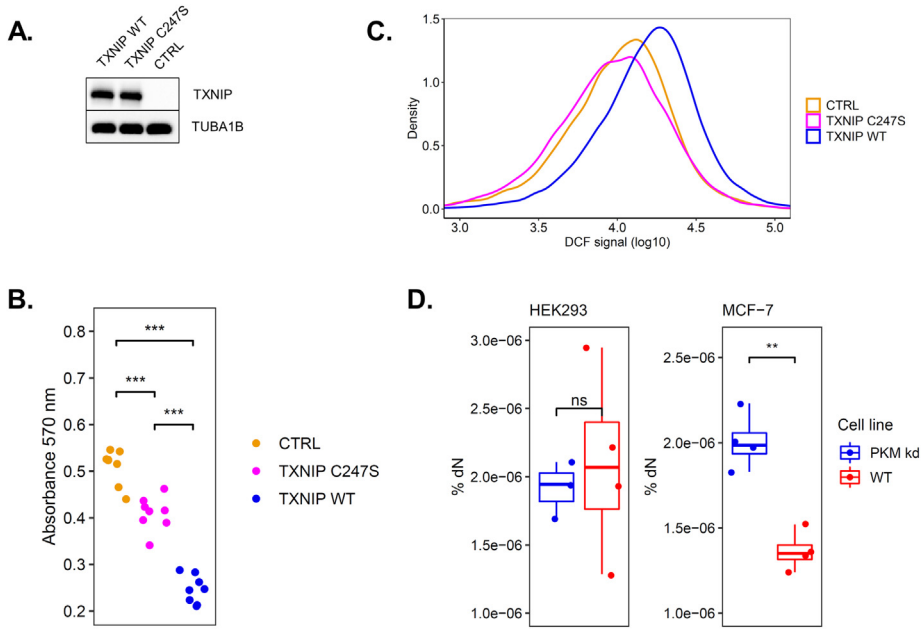

Figure 5: Redox function of TXNIP inhibits cell proliferation and can affect DNA oxidation. (A) Representative immunoblot of total protein extracts in HEK293 transiently transfected with TXNIP WT and mutant TXNIP C247S variants with indicated antibodies. (B) MTT assay representing differences in cell metabolic activity upon transient overexpression of TXNIP WT and TXNIP C247S; n = 8, pairwise Student's t-test, p values adjusted with Bonferroni method, ***$p < 0.001$. (C) Intracellular ROS production in cells transiently overexpressing TXNIP WT or TXNIP C247S measured by flow cytometry to quantify the abundance of a DCF probe. Only overexpression of TXNIP WT leads to the increase of intracellular DCFDA oxidation to DCF (see Supplementary data file 3 for quantification). (D) Comparison of the 8-oxo-dG levels in HEK293 (left) and MCF-7 (right) upon stable PKM knockdown as determined by RT-qPCR n = 4, Student's t-test, ns $p \geq 0.05$, *$p < 0.05$, **$p < 0.01$.

in HEK293 and MCF-7 cell lines. While we did not observe a significant change in the HEK293 model, MCF-7 cells showed significant increase in the levels of oxidised DCFDA (data not shown) as well as of oxidative damage upon PKM knockdown (Figure 5D). Such differences between the two models could be caused by different anti-oxidative systems engaged in ROS scavenging as well as by lower physiological levels of TXNIP in HEK293 in comparison to MCF-7 cells. Indeed, our RNA-seq analysis classified TXNIP in the 60—70% decile and 20—30% decile of genes expressed in WT in MCF-7 and HEK293, respectively. This observation is also consistent with our immunoblotting results (Figure 1C). Altogether, these results suggest that upregulation of TXNIP could result in increased ROS levels and oxidative stress.

3.5. Regulation of TXNIP expression by pyruvate kinase is also observed in metabolically relevant models

We found that PKM depletion triggers TXNIP upregulation in two immortalised, fast-proliferating human cell lines. To investigate whether the newly discovered regulatory PK-TXNIP axis is also present in additional metabolically relevant systems, we decided to validate our findings in two highly glycolytic metabolic models — human HepaRG cells differentiated into hepatocytes, commonly used as a human model to study the regulation of glucose and lipid metabolism [74] and primary mouse hepatocytes. In healthy murine hepatocytes, Pklr is the main isoform of PK, therefore we used a pool of 4 siRNAs targeting the Pklr gene to generate a transient PK knockdown. Three days after siRNA transfection, the amount of Pklr mRNA in samples derived from the mice (n = 3) was significantly reduced (on average to 0.12-fold compared to WT expression). The levels of Txnip were elevated in all samples though the effect size varied between the hepatocytes derived from different animals (Figure 6A). Of note, expression of Pkm was not changed during the course of the experiment (data not shown).

In HepaRG cells, we performed a sequential knockdown of both PKLR and PKM using pools of 4 siRNAs against each transcript. In samples transfected with siRNA against PKLR, TXNIP levels increased on average 1.80- and 1.33-fold in comparison to those transfected with non-targeting control siRNA in single and double knockdowns, respectively (Figure 6B). To further investigate whether the PK-TXNIP regulatory axis is conserved in a full organism, we next analysed zebrafish embryos with a knockout of the two PKM zebrafish orthologs, pkma and pkmb [51]. The zebrafish gene pkma displays similar genomic organisation as the mammalian gene PKM. Its transcript is subjected to alternative splicing giving rise to the processed transcripts pkma1 or pkma2 including exon 9 or 10, respectively [51]. The pkmb transcript is not subjected to alternative splicing and encodes only one isoform [51]. RT-qPCR performed on the RNA extracted from the knockout and wild type zebrafish embryos showed that levels of all pkm transcripts were significantly reduced in the knockout samples, and this reduction correlated with the increase of levels of txnipa and txnipb mRNA (1.13- and 1.62-fold, respectively, in comparison to the wild type embryos (Figure 6C)). These experiments suggest that the PK-TXNIP axis is a versatile effect present in various cell- and animal models.

4. DISCUSSION

Perturbations of glycolysis can result in the misregulation of the metabolic flux through many interconnected pathways and imbalance of metabolites [75—77] and thus can have drastic consequences to the cell and the whole organism. Overexpression of pyruvate kinase (PK), a crucial enzyme in glycolysis, is a hallmark of many human cancers. While the glycolytic role of PK has been implicated in conferring growth advantage of tumour cells over their healthy counterparts, several

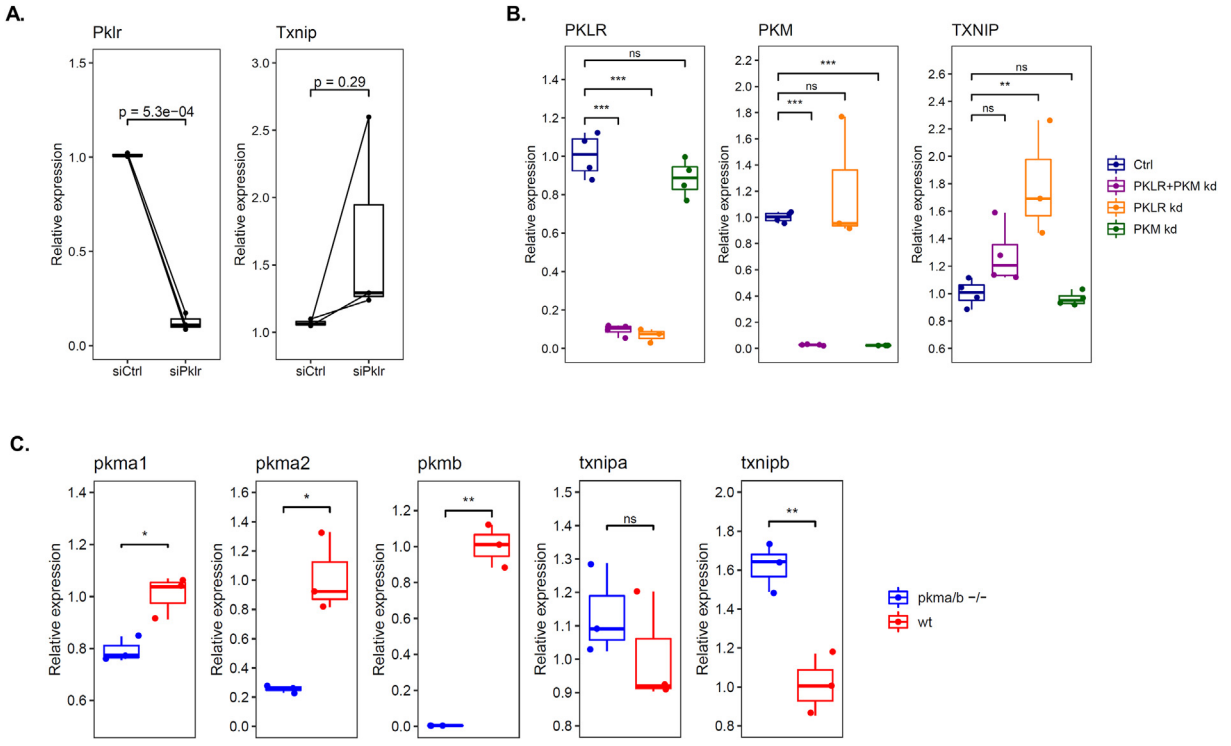

Figure 6: TXNIP upregulation upon depletion of PK activity in different model systems. (A) RT-qPCR quantification of Pklr (left) and Txnip (right) transcripts upon transient siRNA-mediated knockdown of Pklr in mouse primary hepatocytes. Each datapoint represents an average value of 4 technical replicates. Paired samples were derived from the same mouse and treated with non-targeting control or Pklr targeting siRNA; n = 3, Paired samples Student's t-test. (B) RT-qPCR quantification of PKLR (left), PKM (middle) and TXNIP (right) transcripts upon transient sequential siRNA-mediated knockdown of PKLR and/or PKM in HepaRG cells; n = 4, pairwise Student's t-test, p values adjusted with Bonferroni method, ns $p \geq 0.05$, *$p < 0.05$, **$p < 0.01$, ***$p < 0.001$. (C) RT-qPCR quantification of transcripts encoding pkm and txnip variants in wt and pkma/b double knocked out zebrafish embryos (day 5); n = 3, Student's t-test, ns $p \geq 0.05$, *$p < 0.05$, **$p < 0.01$.

other mechanisms involving PK have also been reported to contribute to cancer development [13,14,46]. Here, we provide a metabolic link between impaired enzymatic activity of PK and upregulation of a tumour suppressor TXNIP with potential implications to the cellular ROS balance (Figure 7). How important these effects are on the oncogenic phenotypes of PK inhibition will require further studies. Moreover, we show that this regulatory PK-TXNIP axis is not limited to the immortalised cancer cell lines but is also present in other metabolically-relevant cell- and animal models.

Transcriptional profiling of two fast-proliferating human cell lines, HEK293 and MCF-7, upon shRNA-mediated knockdown of PKM, revealed a significant upregulation of TXNIP and ARRDC4. Expression of both genes has been previously reported to be driven by the glucose-6-phosphate-responsive transcription factors MondoA:MLX [31,33]. This G6P response is also in line with a recent report that pharmacological upregulation of PKM can lead to depletion of TXNIP [78]. Here, we show that PKM depletion changes the flux of glucose-derived compounds and leads to the accumulation of G6P and other glycolytic intermediates, as well as the end products of the pathways branching from glycolysis. We anticipate that similar metabolic changes may be triggered by depletion of other glycolytic enzymes, however the effect size might be different, due to the fact that PK plays a rate-limiting role in glycolysis. Such altered levels of major cellular metabolites have been previously associated with reprogramming the metabolic circuitry and subsequently, global changes of abundance or distribution of chromatin modifications

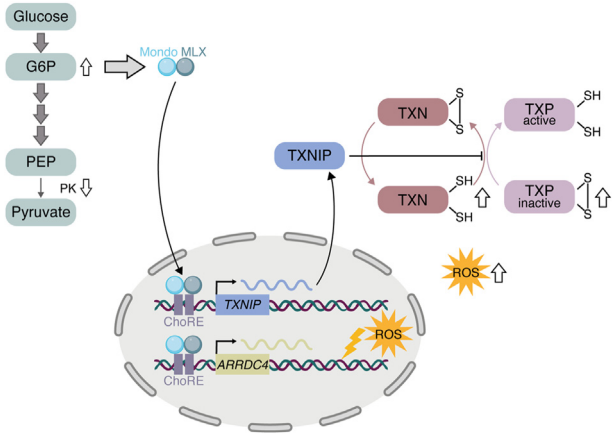

Figure 7: Proposed model of action of PK-TXNIP axis. Upon depletion of PK activity, accumulation of G6P can contribute to increased nuclear localisation of MondoA:MLX heterodimers, their binding to ChoREs and transcriptional upregulation of genes such as TXNIP and ARRDC4. Upregulated TXNIP can bind to and inhibit the reduced form of thioredoxin (TXN) rendering it incapable of reducing oxidised cysteine residues on cellular proteins. Increased level of oxidised thioredoxin peroxidase (TXP) can lead to reduced superoxide anion scavenging capacity and consequently to the accumulation of various ROS that can induce oxidative damage to DNA. Note that beyond the PK-TXNIP axis that we describe here, other stress-related pathways may trigger similar cellular responses. See main text for details.

[79—82]. Surprisingly, even though we detected in our PKM knockdown cells profound changes in the expression of hundreds of genes, our ChIP-seq analysis did not detect major changes in the global histone modification landscape. We rather found a specific gain of active histone marks at specific promoters which correlated with the transcriptional changes, most prominently at the promoters of TXNIP and ARRDC4. This suggests that the supply of metabolites is not the only factor regulating the global deposition of the chromatin marks and that a maintenance mechanisms of the crucial chromatin signatures can exist even upon prolonged metabolic perturbation.

Accumulated glycolytic intermediates can be shunted towards the pathways branching from glycolysis and serve as signalling molecules and metabolic precursors [76]. While in our study we focused on the effects of the direct accumulation of the product of the upstream glycolysis reaction, glucose-6-phosphate, we also detected increased levels of the end products of serine synthesis pathway and pentose phosphate pathway: serine and ribose-5-phosphate, respectively. Therefore, it would be interesting to study the effects of the increased levels of the end products of these and other pathways branching from glycolysis in the future. Intensified flux through the pentose-phosphate pathway might lead to the elevated levels of the reducing equivalent NADPH [83—86]. Apart from its crucial function in synthesis of macromolecules, NADPH significantly contributes to scavenging of cellular ROS by thioredoxins, glutaredoxins and catalase [87—89]. Consequently, it is plausible that in certain cell types and disease models, upon depletion of PK activity, a TXNIP-mediated pro-oxidative state might be compensated by the increased production of NADPH. Such effect could explain why we observed oxidative DNA damage upon PKM knockdown only in MCF-7, in which the base level of TXNIP in WT cells is higher, but not in HEK293 cell line.

Our ChIP profiling revealed a correlation between the PKM knockdown and increased occupancy of carbohydrate-response elements (ChoREs) of TXNIP and ARRDC4 promoters by MondoA and MLX accompanied by the elevation of the levels of active histone marks. While nuclear accumulation of MondoA-MLX heterodimers upon glucose stimulation, as well as a potential role of MondoA in the localised recruitment of histone acetyltransferases to ChoREs, have been previously reported [31,33,90], we show here that a similar effect can be achieved by blocking glycolytic flux by reducing PK activity.

Apart from G6P, TXNIP levels have been previously reported to be elevated in response to multiple compounds implicated in cellular metabolism and differentiation including vitamin D, HDAC inhibitors and mTOR inhibitors [91—97]. Therefore, it is of high interest to further investigate in the future the potential links between the pathways affected by these agents, and PK-mediated modulation of glycolysis in the context of potential additive effects converging on TXNIP upregulation.

TXNIP and its close homolog ARRDC4 have been implicated in regulation of glucose uptake [27,98]. Our results show that beyond this arrestin-specific function in regulating glucose metabolism, upregulated TXNIP can provide an additional level of metabolic control by increasing cellular ROS which correlated with reduced cell proliferation, in line with the findings reported by Patwari et al. [29,99]. Augmented TXNIP expression and elevated ROS production, potentially linked to the increased DNA damage, provides interesting opportunities for designing combination cancer therapies [100,101]. Our work suggests that combining therapeutic agents that trigger ROS-mediated DNA damage with compounds selectively inhibiting PK activity and thereby upregulating tumour suppressor TXNIP, could lead to more efficient killing of fast-proliferating tumour cells. Even though up to now no candidate drugs targeting PK isoforms has been approved for therapy [102], our results provide an additional rationale for further efforts in developing specific inhibitors of PK. However, as a proper balance of PK activity is required for fundamental cellular processes in the whole organism, caution should be taken when designing therapies involving modulation of the activity of this enzyme. For example, PKM1 and PKM2 are central to provide ATP for closing K_{ATP} channels and promoting insulin secretion by pancreatic beta cell and thus could cause additional side effects that would have to be considered [103]. Both PK and TXNIP have been extensively studied separately as an oncogene and a tumour suppressor, respectively. TXNIP displays tumour specific expression and its expression has been suggested as prognostic marker [104]. PKM2 is widely expressed in many types of tumours, has been associated with tumorigenesis and recognised as a potential cancer biomarker [105]. However, the relationship between PK and TXNIP in tumour samples has not been thoroughly investigated. Correlation of expression of PKM and TXNIP genes by using the OncoDB tool [106], revealed specific cancer types with anticorrelated expression (Pearson's $r < -0.25$) of these two genes in the TCGA dataset [107] (Supplementary Table S1). This is accordance with the anticorrelation of expression we observe in our models. Of note, the same dataset reports also positive or no correlation between the expression of PKM and TXNIP in other cancer types. This suggests that the PK-TXNIP regulatory axis is not manifested in every cellular and metabolic background equally and therefore, any therapeutic approach targeting this axis, should be carefully investigated in the context of the specific cancer type.

DECLARATION OF COMPETING INTEREST

The authors declare that they have no known competing financial interests or personal relationships that could have appeared to influence the work reported in this paper.

DATA AVAILABILITY

RNA-seq and ChIP-seq data have been deposited to GEO under accession number GSE235389.

ACKNOWLEDGEMENTS

We thank Didier Stainier for providing the mutant fish lines, Sabine Schlink and Roberto Rojas Rojas for taking care of the fish, Palma Rico Lastres for help with qPCRs and Amelie Kraus for help with Figure 7. Work in the R.S. laboratory was supported by the DFG through SFB 1064 (Project-ID 213249687), SFB 1309 (Project-ID 325871075) and the Helmholtz Gemeinschaft.

The A.Z. laboratory was funded by the German Research Foundation (DFG) grant ZE1037/1-3, EFSD grant 01KU1501C, BMBF grant 16LW0116k, and Marie Sklodowska-Curie ITN, EU Horizon 2020 (EndoConnect).

Work in the lab of UP was supported by the DFG through SFB-TRR179 (project ID 272983813), SFB-TRR388 (project ID 452881907) and the Helmholtz Gemeinschaft.

APPENDIX A. SUPPLEMENTARY DATA

Supplementary data to this article can be found online at https://doi.org/10.1016/j.molmet.2023.101748.

REFERENCES

[1] Vander Heiden MG, DeBerardinis RJ. Understanding the intersections between metabolism and cancer biology. Cell 2017;168(4):657—69. https://doi.org/10.1016/j.cell.2016.12.039.

[2] Vander Heiden MG, Cantley LC, Thompson CB. Understanding the Warburg effect: the metabolic requirements of cell proliferation. Science 2009;324(5930):1029–33. https://doi.org/10.1126/science.1160809.

[3] Vaupel P, Multhoff G. Revisiting the Warburg effect: historical dogma versus current understanding. J Physiol 2021;599(6):1745–57. https://doi.org/10.1113/JP278810.

[4] Warburg O, Wind F, Negelein E. The metabolism of tumours. Br Med J 1927;8(6):519–30. https://doi.org/10.1136/bmj.1.3653.74-a.

[5] Tang Z, Li C, Kang B, Gao G, Li C, Zhang Z. GEPIA: a web server for cancer and normal gene expression profiling and interactive analyses. Nucleic Acids Res 2017;45(W1):W98–102. https://doi.org/10.1093/nar/gkx247.

[6] Feng J, Li J, Wu L, Yu Q, Ji J, Wu J, et al. Emerging roles and the regulation of aerobic glycolysis in hepatocellular carcinoma. J Exp Clin Cancer Res 2020;39(1):1–19. https://doi.org/10.1186/s13046-020-01629-4.

[7] Granchi C, Minutolo F. Anticancer agents that counteract tumor glycolysis. ChemMedChem 2012;7(8):1318–50. https://doi.org/10.1002/cmdc.201200176.

[8] Zahra K, Dey T, Ashish, Mishra SP, Pandey U. Pyruvate kinase M2 and cancer: the role of PKM2 in promoting tumorigenesis. Front Oncol 2020;10(March):1–9. https://doi.org/10.3389/fonc.2020.00159.

[9] Alquraishi M, Puckett DL, Alani DS, Humidat AS, Frankel VD, Donohoe DR, et al. Pyruvate kinase M2: a simple molecule with complex functions. Free Radic Biol Med 2019;143:176–92. https://doi.org/10.1016/j.freeradbiomed.2019.08.007.

[10] Li Z, Yang P, Li Z. The multifaceted regulation and functions of PKM2 in tumor progression. Biochim. Biophys. Acta - Rev. Cancer 2014;1846(2):285–96. https://doi.org/10.1016/j.bbcan.2014.07.008.

[11] Yao A, Xiang Y, Si Y-R, Fan L-J, Li J-P, Li H, et al. PKM2 promotes glucose metabolism through a let-7a-5p/Stat3/hnRNP-A1 regulatory feedback loop in breast cancer cells. J Cell Biochem 2018:1–13. https://doi.org/10.1002/jcb.27947.

[12] Clower CV, Chatterjee D, Wang Z, Cantley LC, Heidena MGV, Krainer AR. The alternative splicing repressors hnRNP A1/A2 and PTB influence pyruvate kinase isoform expression and cell metabolism. Proc Natl Acad Sci USA 2010;107(5):1894–9. https://doi.org/10.1073/pnas.0914845107.

[13] Gao X, Wang H, Yang JJ, Liu X, Liu ZR. Pyruvate kinase M2 regulates gene transcription by acting as a protein kinase. Mol Cell 2012;45(5):598–609. https://doi.org/10.1016/j.molcel.2012.01.001.

[14] Yang W, Xia Y, Hawke D, Li X, Liang J, Xing D, et al. PKM2 phosphorylates histone H3 and promotes gene transcription and tumorigenesis. Cell 2012;150(4):685–96. https://doi.org/10.1016/j.cell.2012.07.018.

[15] Wang HJ, Hsieh YJ, Cheng WC, Lin CP, Lin YS, Yang SF, et al. JMJD5 regulates PKM2 nuclear translocation and reprograms HIF-1α-mediated glucose metabolism. Proc Natl Acad Sci USA 2014;111(1):279–84. https://doi.org/10.1073/pnas.1311249111.

[16] Yang W, Zheng Y, Xia Y, Ji H, Chen X, Guo F., et al. ERK1/2-dependent phosphorylation and nuclear translocation of PKM2 promotes the Warburg effect. Nat Cell Biol 2012;14(12):1295–304. https://doi.org/10.1038/ncb2629.

[17] Salama SA, Mohammad MA, Diaz-Arrastia CR, Kamel MW, Kilic GS, Ndofor BT, et al. Estradiol-17β upregulates pyruvate kinase M2 expression to coactivate estrogen receptor-α and to integrate metabolic reprogramming with the mitogenic response in endometrial cells. J Clin Endocrinol Metab 2014;99(10):3790–9. https://doi.org/10.1210/jc.2013-2639.

[18] Yang W, Lu Z. Nuclear PKM2 regulates the Warburg effect. Cell Cycle 2013;12(19):3343–7. https://doi.org/10.4161/cc.26182.

[19] Christofk HR, Vander Heiden MG, Harris MH, Ramanathan A, Gerszten RE, Wei R., et al. The M2 splice isoform of pyruvate kinase is important for cancer metabolism and tumour growth. Nature 2008;452(7184):230–3. https://doi.org/10.1038/nature06734.

[20] Morita M, Sato T, Nomura M, Sakamoto Y, Inoue Y, Tanaka R, et al. PKM1 confers metabolic advantages and promotes cell-autonomous tumor cell growth. Cancer Cell 2018;33(3):355–367.e7. https://doi.org/10.1016/j.ccell.2018.02.004.

[21] Israelsen WJ, Dayton TL, Davidson SM, Fiske BP, Hosios AM, Bellinger G, et al. PKM2 isoform-specific deletion reveals a differential requirement for pyruvate kinase in tumor cells. Cell 2013;155(2):397. https://doi.org/10.1016/j.cell.2013.09.025.

[22] Hillis AL, Lau AN, Devoe CX, Dayton TL, Danai LV, Di Vizio D, et al. PKM2 is not required for pancreatic ductal adenocarcinoma. Cancer Metabol 2018;6(1):1–8. https://doi.org/10.1186/s40170-018-0188-1.

[23] Wu Q, ba-alawi W, Deblois G, Cruickshank J, Duan S, Lima-Fernandes E, et al. GLUT1 inhibition blocks growth of RB1-positive triple negative breast cancer. Nat Commun 2020;11(1). https://doi.org/10.1038/s41467-020-18020-8.

[24] Zeng K, Ju G, Wang H, Huang J. GLUT1/3/4 as novel biomarkers for the prognosis of human breast cancer. Transl Cancer Res 2020;9(4):2363–77. https://doi.org/10.21037/tcr.2020.03.50.

[25] Waldhart AN, Dykstra H, Peck AS, Boguslawski EA, Madaj ZB, Wen J, et al. Phosphorylation of TXNIP by AKT mediates acute influx of glucose in response to insulin. Cell Rep 2017;19(10):2005–13. https://doi.org/10.1016/j.celrep.2017.05.041.

[26] Wu N, Zheng B, Shaywitz A, Dagon Y, Tower C, Bellinger G, et al. AMPK-dependent degradation of TXNIP upon energy stress leads to enhanced glucose uptake via GLUT1. Mol Cell 2013;49(6):1167–75. https://doi.org/10.1016/j.molcel.2013.01.035.

[27] Patwari P, Lee RT. An expanded family of arrestins regulate metabolism. Trends Endocrinol Metabol 2012;23(5):216–22. https://doi.org/10.1016/j.tem.2012.03.003.

[28] Alhawiti NM, Al Mahri S, Aziz MA, Malik SS, Mohammad S. TXNIP in metabolic regulation: physiological role and therapeutic outlook. Curr Drug Targets 2017;18(9):1095–103. https://doi.org/10.2174/1389450116866170130145514.

[29] Patwari P, Higgins LJ, Chutkow WA, Yoshioka J, Lee RT. The interaction of thioredoxin with Txnip: evidence for formation of a mixed disulfide by disulfide exchange. J Biol Chem 2006;281(31):21884–91. https://doi.org/10.1074/jbc.M600427200.

[30] Minn AH, Hafele C, Shalev A. Thioredoxin-interacting protein is stimulated by glucose through a carbohydrate response element and induces β-cell apoptosis. Endocrinology 2005;146(5):2397–405. https://doi.org/10.1210/en.2004-1378.

[31] Stoltzman CA, Peterson CW, Breen KT, Muoio DM, Billin AN, Ayer DE. Glucose sensing by MondoA:Mlx complexes: a role for hexokinases and direct regulation of thioredoxin-interacting protein expression. Proc Natl Acad Sci USA 2008;105(19):6912–7. https://doi.org/10.1073/pnas.0712199105.

[32] Lee S, Kim SM, Lee RT. Thioredoxin and thioredoxin target proteins: from molecular mechanisms to functional significance. Antioxidants Redox Signal 2013;18(10):1165–207. https://doi.org/10.1089/ars.2011.4322.

[33] Peterson CW, Stoltzman CA, Sighinolfi MP, Han KS, Ayer DE. Glucose controls nuclear accumulation, promoter binding, and transcriptional activity of the MondoA-Mlx heterodimer. Mol Cell Biol 2010;30(12):2887–95. https://doi.org/10.1128/mcb.01613-09.

[34] Cha-Molstad H, Saxena G, Chen J, Shalev A. Glucose-stimulated expression of Txnip is mediated by carbohydrate response element-binding protein, p300, and histone H4 acetylation in pancreatic beta cells. J Biol Chem 2009;284(25):16898–905. https://doi.org/10.1074/jbc.M109.010504.

[35] Richards P, Rachdi L, Oshima M, Marchetti P, Bugliani M, Armanet M, et al. MondoA is an essential glucose-responsive transcription factor in human pancreatic β-cells. Diabetes 2018;67(3):461–72. https://doi.org/10.2337/db17-0595.

[36] Kim SY, Suh HW, Chung JW, Yoon SR, Choi I. Diverse functions of VDUP1 in cell proliferation, differentiation, and diseases. Cell Mol Immunol 2007;4(5):345–51.

[37] Nishiyama A, Matsui M, Iwata S, Hirota K, Masutani H, Nakamura H, et al. Identification of thioredoxin-binding protein-2/vitamin D3 up-regulated protein 1 as a negative regulator of thioredoxin function and expression. J Biol Chem 1999;274(31):21645–50. https://doi.org/10.1074/jbc.274.31.21645.

[38] Junn E, Han SH, Im JY, Yang Y, Cho EW, Um HD, et al. Vitamin D 3 up-regulated protein 1 mediates oxidative stress via suppressing the thioredoxin function. J Immunol 2000;164(12):6287–95. https://doi.org/10.4049/jimmunol.164.12.6287.

[39] Zhang M, Hu G, Shao N, Qin Y, Chen Q, Wang Y, et al. Thioredoxin-interacting protein (TXNIP) as a target for Alzheimer's disease: flavonoids and phenols. Inflammopharmacology 2021. https://doi.org/10.1007/s10787-021-00861-4.

[40] Domingues A, Jolibois J, de Rougé PM, Nivet-Antoine V. The emerging role of TXNIP in ischemic and cardiovascular diseases; a novel marker and therapeutic target. Int J Mol Sci 2021;22(4):1–25. https://doi.org/10.3390/ijms22041693.

[41] Tsubaki H, Tooyama I, Walker DG. Thioredoxin-interacting protein (TXNIP) with focus on brain and neurodegenerative diseases. Int J Mol Sci 2020;21(24). https://doi.org/10.3390/ijms21249357.

[42] Yoshihara E. In: TXNIP/TBP-2 : a master regulator for glucose homeostasis, vol. 3; 2020. p. 1–20.

[43] Chen Y, Ning J, Cao W, Wang S, Du T, Jiang J, et al. Research progress of TXNIP as a tumor suppressor gene participating in the metabolic reprogramming and oxidative stress of cancer cells in various cancers. Front Oncol 2020;10(October):1–12. https://doi.org/10.3389/fonc.2020.568574.

[44] Zhou J, Chng WJ. Roles of thioredoxin binding protein (TXNIP) in oxidative stress, apoptosis and cancer. Mitochondrion 2013;13(3):163–9. https://doi.org/10.1016/j.mito.2012.06.004.

[45] Zhou J, Yu Q, Chng WJ. TXNIP (VDUP-1, TBP-2): a major redox regulator commonly suppressed in cancer by epigenetic mechanisms. Int J Biochem Cell Biol 2011;43(12):1668–73. https://doi.org/10.1016/j.biocel.2011.09.005.

[46] Yu Q, Tong C, Luo M, Xue X, Mei Q, Ma L, et al. Regulation of SESAME-mediated H3T11 phosphorylation by glycolytic enzymes and metabolites. PLoS One 2017;12(4):1–15. https://doi.org/10.1371/journal.pone.0175576.

[47] Palsson-McDermott EM, Dyck L, Zaslona Z, Menon D, McGettrick AF, Mills KHG, et al. Pyruvate kinase M2 is required for the expression of the immune checkpoint PD-L1 in immune cells and tumors. Front Immunol 2017;8. https://doi.org/10.3389/fimmu.2017.01300.

[48] Zellmer S, Schmidt-Heck W, Godoy P, Weng H, Meyer C, Lehmann T, et al. Transcription factors ETF, E2F, and SP-1 are involved in cytokine-independent proliferation of murine hepatocytes. Hepatology 2010;52(6):2127–36. https://doi.org/10.1002/hep.23930.

[49] Sekar R, Motzler K, Kwon Y, Novikoff A, Jülg J, Najafi B, et al. Vps37a regulates hepatic glucose production by controlling glucagon receptor localization to endosomes. Cell Metabol 2022;34(11):1824–1842.e9. https://doi.org/10.1016/j.cmet.2022.09.022.

[50] Kimmel CB, Ballard WW, Kimmel SR, Ullmann B, Schilling TF. Stages of embryonic development of the zebrafish. Dev Dynam 1995;203(3):253–310. https://doi.org/10.1002/aja.1002030302.

[51] Stone OA, El-Brolosy M, Wilhelm K, Liu X, Romão AM, Grillo E, et al. Loss of pyruvate kinase M2 limits growth and triggers innate immune signaling in endothelial cells. Nat Commun 2018;9(1):4077. https://doi.org/10.1038/s41467-018-06406-8.

[52] D'Amico L, Scott IC, Jungblut B, Stainier DYR. A mutation in zebrafish hmgcr1b reveals a role for isoprenoids in vertebrate heart-tube formation. Curr Biol 2007;17(3):252–9. https://doi.org/10.1016/j.cub.2006.12.023.

[53] Krueger F, James F, Ewels P, Afyounian E, Schuster-Boeckler B. FelixKrueger/TrimGalore: v0.6.7 - DOI via Zenodo. Zenodo. 2021. https://doi.org/10.5281/zenodo.5127899.

[54] Stolarczyk M, Reuter VP, Smith JP, Magee NE, Sheffield NC. Refgenie: a reference genome resource manager. GigaScience 2020;9(2). https://doi.org/10.1093/gigascience/giz149.

[55] Patro R, Duggal G, Love MI, Irizarry RA, Kingsford C. Salmon provides fast and bias-aware quantification of transcript expression. Nat Methods 2017;14(4):417–9. https://doi.org/10.1038/nmeth.4197.

[56] Love MI, Huber W, Anders S. Moderated estimation of fold change and dispersion for RNA-seq data with DESeq2. Genome Biol 2014;15(12):1–21. https://doi.org/10.1186/s13059-014-0550-8.

[57] Harrison PF, Pattison AD, Powell DR, Beilharz TH. Topconfects: a package for confident effect sizes in differential expression analysis provides a more biologically useful ranked gene list. Genome Biol 2019;20(1):67. https://doi.org/10.1186/s13059-019-1674-7.

[58] Capellades J, Junza A, Samino S, Brunner JS, Schabbauer G, Vinaixa M, et al. Exploring the use of gas chromatography coupled to chemical ionization mass spectrometry (GC-CI-MS) for stable isotope labeling in metabolomics. Anal Chem 2021;93(3):1242–8.

[59] Schelter F, Kirchner A, Traube FR, Müller M, Steglich W, Carell T. 5-Hydroxymethyl-, 5-formyl- and 5-carboxydeoxycytidines as oxidative lesions and epigenetic marks. Chem Eur J 2021;27(31):8100–4. https://doi.org/10.1002/chem.202100551.

[60] Oda A, Takemata N, Hirata Y, Miyoshi T, Suzuki Y, Sugano S, et al. Dynamic transition of transcription and chromatin landscape during fission yeast adaptation to glucose starvation. Gene Cell 2015;20(5):392–407. https://doi.org/10.1111/gtc.12229.

[61] Alcántar-Fernández J, Navarro RE, Salazar-Martínez AM, Pérez-Andrade ME, Miranda-Ríos J. Caenorhabditis elegans respond to high-glucose diets through a network of stress-responsive transcription factors. PLoS One 2018;13(7):e0199888. https://doi.org/10.1371/journal.pone.0199888.

[62] Zhou C, Qian W, Li J, Ma J, Chen X, Jiang Z, et al. High glucose microenvironment accelerates tumor growth via SREBP1-autophagy axis in pancreatic cancer. J Exp Clin Cancer Res 2019;38(1):302. https://doi.org/10.1186/s13046-019-1288-7.

[63] Enzo E, Santinon G, Pocaterra A, Aragona M, Bresolin S, Forcato M, et al. Aerobic glycolysis tunes YAP/TAZ transcriptional activity. EMBO J 2015;34(10):1349–70. https://doi.org/10.15252/embj.201490379.

[64] Cilenti L, Di Gregorio J, Ambivero CT, Andl T, Liao R, Zervos AS. Mitochondrial MUL1 E3 ubiquitin ligase regulates Hypoxia Inducible Factor (HIF-1α) and metabolic reprogramming by modulating the UBXN7 cofactor protein. Sci Rep 2020;10(1):1–15. https://doi.org/10.1038/s41598-020-58484-8.

[65] Romero N, Swain PM, Kam Y, Rogers G, Drank BP. Bioenergetic profiling of cancer cell lines: quantifying the impact of glycolysis on cell proliferation. In: AACR Annual Meeting; 2018. https://doi.org/10.1158/1538-7445.AM2018-3487.

[66] Christofk HR, Vander Heiden MG, Wu N, Asara JM, Cantley LC. Pyruvate kinase M2 is a phosphotyrosine-binding protein. Nature 2008;452:181–6.

[67] Wang X, Zhang F, Wu XR. Inhibition of pyruvate kinase M2 markedly reduces chemoresistance of advanced bladder cancer to cisplatin. no. December 2016 Sci Rep 2017;7:1–13. https://doi.org/10.1038/srep45983.

[68] Orlando DA, Chen MW, Brown VE, Solanki S, Choi YJ, Olson ER, et al. Quantitative ChIP-seq normalization reveals global modulation of the epigenome. Cell Rep 2014;9(3):1163–70. https://doi.org/10.1016/j.celrep.2014.10.018.

[69] Parmenter TJ, Kleinschmidt M, Kinross KM, Bond ST, Li J, Kaadige MR, et al. Response of BRAF mutant melanoma to BRAF inhibition is mediated by a network of transcriptional regulators of glycolysis. Cancer Discov 2014;4(4):423–33. https://doi.org/10.1158/2159-8290.CD-13-0440.

[70] Ge T, Yang J, Zhou S, Wang Y, Li Y, Tong X. The role of the pentose phosphate pathway in diabetes and cancer. no. June Front Endocrinol 2020;11:1–11. https://doi.org/10.3389/fendo.2020.00365.

[71] Wu Q, Chen X, Li J, Sun S. Serine and metabolism regulation: a novel mechanism in antitumor immunity and senescence. Aging Dis 2020;11(6):1640–53. https://doi.org/10.14336/AD.2020.0314.

[72] Muoio DM. TXNIP links redox circuitry to glucose control. Cell Metabol 2007;5(6):412–4. https://doi.org/10.1016/j.cmet.2007.05.011.

[73] Rani S, Mehta JP, Barron N, Doolan P, Jeppesen PB, Clynes M, et al. Decreasing Txnip mRNA and protein levels in pancreatic MIN6 cells reduces reactive oxygen species and restores glucose regulated insulin secretion. Cell Physiol Biochem 2010;25(6):667–74. https://doi.org/10.1159/000315086.

[74] Samanez CH, Caron S, Briand O, Dehondt H, Duplan I, Kuipers F, et al. The human hepatocyte cell lines IHH and HepaRG: models to study glucose, lipid and lipoprotein metabolism. Arch Physiol Biochem 2012;118(3):102–11. https://doi.org/10.3109/13813455.2012.683442.

[75] Lunt SY, Vander Heiden MG. Aerobic glycolysis: meeting the metabolic requirements of cell proliferation. Annu Rev Cell Dev Biol 2011;27:441–64. https://doi.org/10.1146/annurev-cellbio-092910-154237.

[76] Ryan DG, Murphy MP, Frezza C, Prag HA, Chouchani ET, O'Neill LA, et al. Coupling Krebs cycle metabolites to signalling in immunity and cancer. Nature Metabolism 2019;1(1):16. https://doi.org/10.1038/s42255-018-0014-7.

[77] Li L, Fath MA, Scarbrough PM, Watson WH, Spitz DR. Combined inhibition of glycolysis, the pentose cycle, and thioredoxin metabolism selectively increases cytotoxicity and oxidative stress in human breast and prostate cancer. Redox Biol 2015;4:127–35. https://doi.org/10.1016/j.redox.2014.12.001.

[78] Almouhanna F, Blagojevic B, Can S, Ghanem A, Wölfl S. Pharmacological activation of pyruvate kinase M2 reprograms glycolysis leading to TXNIP depletion and AMPK activation in breast cancer cells. Cancer Metabol 2021;9(1):1–17. https://doi.org/10.1186/s40170-021-00239-8.

[79] Mentch SJ, Mehrmohamadi M, Huang L, Liu X, Gupta D, Mattocks D, et al. Histone methylation dynamics and gene regulation occur through the sensing of one-carbon metabolism. Cell Metabol 2015;22(5):861–73. https://doi.org/10.1016/j.cmet.2015.08.024.

[80] Cluntun AA, Huang H, Dai L, Liu X, Zhao Y, Locasale JW. The rate of glycolysis quantitatively mediates specific histone acetylation sites. Cancer Metabol 2015;3(1):10. https://doi.org/10.1186/s40170-015-0135-3.

[81] Ganapathy-Kanniappan S, Geschwind J-F. Tumor glycolysis as a target for cancer therapy. Mol Cancer 2013;12(1):1–11.

[82] Amelio I, Cutruzzolá F, Antonov A, Agostini M, Melino G. Serine and glycine metabolism in cancer. Trends Biochem Sci 2014;39(4):191–8. https://doi.org/10.1016/j.tibs.2014.02.004.

[83] Tian WN, Braunstein LD, Pang J, Stuhlmeier KM, Xi QC, Tian X, et al. Importance of glucose-6-phosphate dehydrogenase activity for cell growth. J Biol Chem 1998;273(17):10609–17. https://doi.org/10.1074/jbc.273.17.10609.

[84] Tuttle S, Stamato T, Perez ML, Biaglow J. Glucose-6-phosphate dehydrogenase and the oxidative pentose phosphate cycle protect cells against apoptosis induced by low doses of ionizing radiation. Radiat Res Jun. 2000;153(6):781–7. https://doi.org/10.1667/0033-7587(2000)153[0781:gpdato]2.0.co;2.

[85] Pandolfi PP, Sonati F, Rivi R, Mason P, Grosveld F, Luzzatto L. Targeted disruption of the housekeeping gene encoding glucose 6-phosphate dehydrogenase (G6PD): G6PD is dispensable for pentose synthesis but essential for defense against oxidative stress. EMBO J 1995;14(21):5209–15. https://doi.org/10.1002/j.1460-2075.1995.tb00205.x.

[86] Mullarky E, Cantley LC. Diverting glycolysis to combat oxidative stress. In: Innovative medicine; 2015. p. 3–23.

[87] Ahsan MK, Lekli I, Ray D, Yodoi J, Das DK. Redox regulation of cell survival by the thioredoxin superfamily: an implication of redox gene therapy in the heart. Antioxidants Redox Signal 2009;11(11):2741–58. https://doi.org/10.1089/ars.2009.2683.

[88] Ju HQ, Lin JF, Tian T, Xie D, Xu RH. NADPH homeostasis in cancer: functions, mechanisms and therapeutic implications. Signal Transduct Targeted Ther 2020;5(1):1–12. https://doi.org/10.1038/s41392-020-00326-0.

[89] Karlenius TC, Tonissen KF. Thioredoxin and cancer: a role for thioredoxin in all states of tumor oxygenation. Cancers 2010;2(2):209–32. https://doi.org/10.3390/cancers2020209.

[90] Wilde BR, Ye Z, Lim T-Y, Ayer DE. Cellular acidosis triggers human MondoA transcriptional activity by driving mitochondrial ATP production. Elife 2019;8:1–25. https://doi.org/10.7554/eLife.40199.

[91] Zhang B, Lyu J, Yang EJ, Liu Y, Wu C, Pardeshi L, et al. Class I histone deacetylase inhibition is synthetic lethal with BRCA1 deficiency in breast cancer cells. Acta Pharm Sin B 2020;10(4):615–27. https://doi.org/10.1016/j.apsb.2019.08.008.

[92] Malone CF, Emerson C, Ingraham R, Barbosa W, Guerra S, Yoon H, et al. mTOR and HDAC inhibitors converge on the TXNIP/thioredoxin pathway to cause catastrophic oxidative stress and regression of RAS-driven tumors. Cancer Discov 2017;7(12):1450–63. https://doi.org/10.1158/2159-8290.CD-17-0177.

[93] Bridgeman S, Ellison G, Newsholme P, Mamotte C. The HDAC inhibitor butyrate impairs β cell function and activates the disallowed gene hexokinase I. Int J Mol Sci 2021;22(24). https://doi.org/10.3390/ijms222413330.

[94] Yamato E. High dose of histone deacetylase inhibitors affects insulin secretory mechanism of pancreatic beta cell line. Endocr Regul 2018;52(1):21–6. https://doi.org/10.2478/enr-2018-0004.

[95] Feingold PL, Surman DR, Brown K, Xu Y, McDuffie LA, Shukla V, et al. Induction of thioredoxin-interacting protein by a histone deacetylase inhibitor, entinostat, is associated with DNA damage and apoptosis in esophageal adenocarcinoma. Mol Cancer Therapeut 2018;17(9):2013–23. https://doi.org/10.1158/1535-7163.MCT-17-1240.

[96] Elgort MG, O'Shea JM, Jiang Y, Ayer DE. Transcriptional and translational downregulation of thioredoxin interacting protein is required for metabolic reprogramming during G1. Genes and Cancer 2010;1(9):893–907. https://doi.org/10.1177/1947601910389604.

[97] Chau GC, Im DU, Kang TM, Bae JM, Kim W, Pyo S, et al. mTOR controls ChREBP transcriptional activity and pancreatic β cell survival under diabetic stress. J Cell Biol 2017;216(7):2091–105. https://doi.org/10.1083/jcb.201701085.

[98] Parikh H, Carlsson E, Chutkow WA, Johansson LE, Storgaard H, Poulsen P, et al. TXNIP regulates peripheral glucose metabolism in humans. PLoS Med 2007;4(5):868–79. https://doi.org/10.1371/journal.pmed.0040158.

[99] Patwari P, Chutkow WA, Cummings K, Verstraeten VLRM, Lammerding J, Schreiter ER, et al. Thioredoxin-independent regulation of metabolism by the α-arrestin proteins. J Biol Chem 2009;284(37):24996–5003. https://doi.org/10.1074/jbc.M109.018093.

[100] Mokhtari RB, Homayouni TS, Baluch N, Morgatskaya E, Kumar S, Das B, et al. Combination therapy in combating cancer. Oncotarget 2017;8(23):38022–43.

[101] Kanaji N, Kamitori K, Hossain A, Noguchi C, Katagi A, Kadowaki N, et al. Additive antitumour effect of D-allose in combination with cisplatin in non-small cell lung cancer cells. Oncol Rep 2018;39(3):1292–8. https://doi.org/10.3892/or.2018.6192.

[102] Chen J, Xie J, Jiang Z, Wang B, Wang Y, Hu X. Shikonin and its analogs inhibit cancer cell glycolysis by targeting tumor pyruvate kinase-M2. Oncogene 2011;30(42):4297–306. https://doi.org/10.1038/onc.2011.137.

[103] Foster HR, Ho T, Potapenko E, Sdao SM, Huang SM, Lewandowski SL, et al. β-cell deletion of the PKm1 and PKm2 isoforms of pyruvate kinase in mice reveals their essential role as nutrient sensors for the KATP channel. Elife 2022;11. https://doi.org/10.7554/ELIFE.79422.

[104] Guo X, Huang M, Zhang H, Chen Q, Hu Y, Meng Y, et al. A pan-cancer analysis of thioredoxin-interacting protein as an immunological and prognostic biomarker. Cancer Cell Int 2022;22(1):1–16. https://doi.org/10.1186/s12935-022-02639-2.

[105] Chen X, Chen S, Yu D. Protein kinase function of pyruvate kinase M2 and cancer. Cancer Cell Int 2020;20(1):1–11. https://doi.org/10.1186/s12935-020-01612-1.

[106] Tang G, Cho M, Wang X. OncoDB: an interactive online database for analysis of gene expression and viral infection in cancer. Nucleic Acids Res 2022;50(D1):D1334–9. https://doi.org/10.1093/nar/gkab970.

[107] The Cancer Genome Atlas Research Network, Weinstein JN, Collisson EA, Mills GB, Shaw KRM, Ozenberger BA, et al. The cancer genome atlas pan-cancer analysis project. Nat Genet 2013;45(10):1113–20. https://doi.org/10.1038/ng.2764.

